



Highly efficient activation of peroxymonosulfate by natural negatively-charged kaolinite with abundant hydroxyl groups for the degradation of atrazine



Chunquan Li^{a,b}, Ying Huang^b, Xiongbo Dong^a, Zhiming Sun^{a,*}, Xiaodi Duan^b, Bangxing Ren^b, Shuilin Zheng^{a,*}, Dionysios D. Dionysiou^{b,*}

^a School of Chemical and Environmental Engineering, China University of Mining and Technology (Beijing), Beijing, 100083, PR China

^b Department of Chemical and Environmental Engineering (DCEE), University of Cincinnati, Cincinnati, OH, 45221-0012, USA

ARTICLE INFO

Keywords:

Kaolinite
Atrazine
Peroxymonosulfate
Sulfate radical
Hydroxyl radical

ABSTRACT

In this study, natural kaolinite, an abundant, low cost, thermally and chemically stable, and easily recyclable material was evaluated for the performance to activate peroxymonosulfate (PMS) by the degradation of atrazine. Based on radical quenching experiments and electron spinning resonance (ESR) spectra, hydroxyl radical ($\cdot\text{OH}$) and sulfate radical ($\text{SO}_4^{\cdot-}$) were identified to be the primary reactive species. The effects of catalyst loading, initial reaction pH, PMS dosage, initial atrazine concentration, and the presence of inorganic ions (Cl^- , NO_3^- , HCO_3^- and H_2PO_4^-) were also investigated in this work. Interestingly, the presence of H_2PO_4^- enhanced the degradation efficiency of atrazine via promoting the decomposition of PMS. The transformation products were detected on a quadrupole time-of-flight liquid chromatography/mass spectrometer (Q-TOF-LC-MS) and the possible degradation pathway of atrazine was proposed. Based on comprehensive characterizations of crystal phase and crystallinity, porosity and pore structure, surface morphology, functional groups, and valence state of specific elements, the catalytic ability of natural kaolinite towards PMS is attributed to the abundant surface-bonded and structural hydroxyl groups. This study provides new insights of PMS activation by natural minerals for the degradation of refractory and deleterious contaminants in wastewater treatment.

1. Introduction

Water resource scarcity has caused extensive public concern [1] since various chemicals including pesticides, antibiotics, heavy metals and toxins are not efficiently removed in the water treatment processes, which poses serious threat to human health. Several processes including membrane filtration, chemical oxidation, physical adsorption, and biological degradation have been applied for water treatment over the years. Nevertheless, these technologies are generally facing certain drawbacks such as intensive energy consumption, incomplete treatment capabilities, high cost, or low purification efficiencies, thus further remediation is required in many cases [2–5]. Recently, advanced oxidation processes (AOPs) have exhibited promising prospects in certain applications for water treatment because of their capacity to achieve effective degradation of recalcitrant compounds that are not efficiently removed by traditional methods [6–8].

Sulfate radical ($\text{SO}_4^{\cdot-}$) based-AOPs can effectively degrade various organic contaminants due to the high standard redox potential

(2.5–3.1 V) and good reactivity of sulfate radical and wide responding pH range (3–8) of such technologies [9]. $\text{SO}_4^{\cdot-}$ can be efficiently generated via the activation of PMS homogeneously using transition metal ions (Co^{2+} , Ce^{3+} , Ag^+ , Fe^{2+} , Fe^{3+} , Ni^{2+} , Ru^{3+} , Mn^{2+} , etc.) or heterogeneously using metal oxides (manganese oxides, cobalt oxides, zinc ferrite, or other supported metal catalysts) [10–12]. However, these processes are generally carried out in the presence of heavy metal ions or suffering from metal leaching, which might cause secondary water contamination. Besides, these heterogeneous catalysts or metal ions are difficult to be recycled due to the nano dimension of the particle size or ionic form. Therefore, developing new catalysts which can reduce the influence of heavy metal ions are “green” strategies for water remediation. Recently, some literature studies reported that N-doped graphene, N-doped carbon nanotubes, and N-doped graphitic biochar could be used to activate PMS based on electron transfer. Nevertheless, the preparation process of these materials might also be complex and energy-intensive [13–15]. Furthermore, although UV, heat, ultrasound and electro-chemical methods can activate PMS to

* Corresponding authors.

E-mail addresses: zhimingsun@cumtb.edu.cn (Z. Sun), zhengsl@cumtb.edu.cn (S. Zheng), dionysios.d.dionysiou@uc.edu (D.D. Dionysiou).

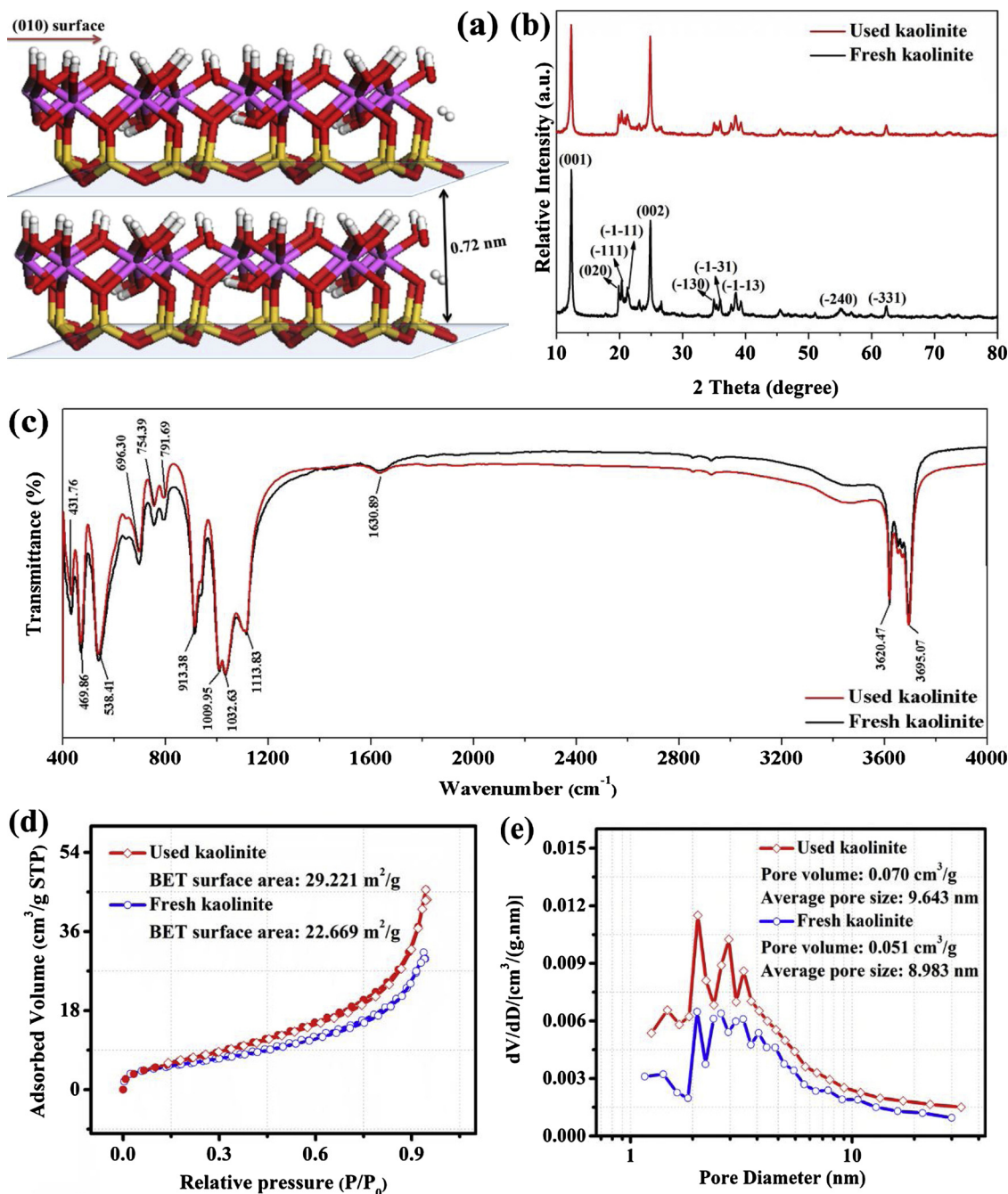


Fig. 1. (a) Crystal structure of kaolinite, (b–e) XRD, FTIR, Nitrogen isotherm adsorption-desorption curves and Pore size distribution curves of fresh and used kaolinite.

some extent as well, high cost and complicated operation are also the obstacles for them to realize commercialization [16–18]. Thus, exploring environmental-friendly materials which can activate PMS effectively without the assistance of other energy source (light, sound, heat, electricity, etc.) is an important research area of PMS catalysis.

It is well-known that natural minerals have been wildly utilized because of their abundance, low cost, high adsorption capacity, thermal and chemical stability, and easy recycling [19–21]. Among various natural minerals, kaolinite is one typical two-dimensional (2D) layered mineral, composed of one sheet of silicon-oxygen tetrahedron and one sheet of aluminum-oxygen octahedron (Fig. 1(a)). The abundant surface-bonded and structural hydroxyl groups, rich adsorption sites, and micron dimension make kaolinite a promising catalyst for the activation of PMS.

In our present work, we used the natural kaolinite to catalyze PMS with the generation of reactive species for the first time. The variance of crystalline property, porosity structure, surface morphology, functional groups and valence state of specific elements of kaolinite before and after the reaction were comprehensively investigated. Atrazine (ATZ), as one of dangerous herbicides that has been frequently detected in water resources and wastewater, was used as the target contaminant to test the activation efficiency of kaolinite for PMS. The impacts of catalyst loading, initial pH, PMS dosage, initial atrazine concentration, and the presence of inorganic ions (Cl^- , NO_3^- , HCO_3^- and H_2PO_4^-) on atrazine degradation were also explored. The possible degradation pathways of atrazine by kaolinite/PMS were illustrated based on the detected transformation products. This study provides a new strategy for PMS activation using natural kaolinite and a fundamental

understanding about the reaction mechanisms during the atrazine degradation for possible applications in wastewater treatment.

2. Experimental

2.1. Materials and chemical reagents

Natural kaolinite used in this study was produced in Suzhou City, China. Atrazine ($C_9H_{17}N_5O$, 97%), potassium peroxymonosulfate (PMS, $2KHSO_5 \cdot KHSO_4 \cdot K_2SO_4$, 95%), iron nitrate nonahydrate ($Fe(NO_3)_3 \cdot 9H_2O$, 98%) and iron chloride hexahydrate ($FeCl_3 \cdot 6H_2O$, 97%) were purchased from Sigma-Aldrich Company (St. Louis, MO, USA). Tertiary-butanol (TBA), acetonitrile (HPLC grade), methanol (HPLC grade), potassium hydroxide (KOH, 85%), sodium thiosulfate ($Na_2S_2O_3 \cdot 5H_2O$, 99%), potassium bicarbonate ($KHCO_3$, 99.5%), potassium dihydrogen phosphate (KH_2PO_4 , 99%), hydrochloric acid (HCl, 36.5%), potassium nitrate (KNO_3 , 99%), potassium chloride (KCl, 99.5%), and aluminum sulfate hexadecahydrate ($Al_2(SO_4)_3 \cdot 12H_2O$, 98%) were obtained from Fisher Scientific (Pittsburgh, PA, USA). Pure ethanol (EtOH) was bought from Decon Laboratories Inc. (King of Prussia, PA, USA). Suwannee River Natural Organic Matter (NOM) standard (RO isolate) was purchased from the International Humic Substances Society (MN, US). The NOM stock solution was prepared in a method same with our previous report [22]. Ultra-purified water was used through all experiment procedures (resistivity $\geq 18.2\text{ M}\Omega\text{ cm}$, Millipore, Watford, UK).

2.2. Characterizations

The crystal phase and structure of kaolinite were analyzed by a Bruker D8 X-ray diffractometer (XRD) (Bruker-AXS, Germany). The surface properties and morphology of kaolinite were investigated by an S-4800 field emission scanning electron microscopy (FESEM) (Hitachi, Japan). The Brunauer–Emmett–Teller (BET) surface area and Barrett–Joyner–Halenda (BJH) pore size distribution was assessed by a JW-BK nitrogen adsorption-desorption isotherm analyzer apparatus (JWGB Sci. & Tech, Beijing) at 77 K. Fourier-transform infrared spectroscopy (FTIR) (Nicolet 6700) with KBr pellet was used to measure the valence bonding and functional group of materials. The kaolinite and kaolinite/PMS in water matrix were detected by a Bruker VERTEX70 FTIR analyzer. A Thermo ESCALAB 250Xi X-ray photoelectron spectrometer (XPS) was employed to measure the spectra of kaolinite by using an Al K α monochromatized source. Shirley background and Gaussian Lorentzian fitting were used to change peak intensities and areas. The reactive species during the dark degradation process were detected by a JEOL FA-200 electron spin resonance spectrometer. The zeta potential of natural kaolinite was measured using a Mastersizer 2000 Malvern laser particle size analyzer. XRF-1800 (Shimadzu, Japan) was employed to detect the elemental composition of kaolinite. A TOC-L analyzer (Shimadzu, Japan) was used to analyze the total organic carbon (TOC). The leaching elements content was quantified by an Agilent 7500ce inductively coupled plasma-mass spectrometry (ICP-MS). NH₃-TPD was tested by an AutoChem II 2920 instrument. An iodometric titration method was used to measure the concentration of residual PMS after reactions [23].

2.3. PMS activation and atrazine degradation

In this study, experiments were conducted by using brown vial with a volume of 40 mL. In a general experiment procedure, kaolinite powder (mean diameter 4.59 μm) was firstly poured into atrazine solution (4.6 μM , 30 mL), then 1 mL freshly prepared PMS solution (30 mM) was added. The pH of reaction solution decreased to 3.4 after adding 1 mM of PMS. Afterwards, these samples were shaken by a numerical control rotary mixer (MX-RL-Pro, SCILOGEX) to start the reaction. When the initial reactions started, 200 μL samples were taken

at specific time of 5, 10, 15, 30, 60, 90 and 120 min, and quenched by methanol (34.7 M) and sodium thiosulfate (1.0 M) immediately, and then filtered by 0.2 μm PES water membrane filter (Jinlong Co., Tianjin, China). Finally, high-performance liquid chromatography (HPLC) was used to analyze the concentration of atrazine as illustrated in Text S1. All experiments were conducted in parallel.

2.4. The steady state concentrations of SO_4^{2-} and $\cdot OH$

To explore the steady state concentration of SO_4^{2-} and $\cdot OH$ within the kaolinite/PMS/H₂PO₄⁻ system ($[SO_4^{2-}]_{ss}$ and $[\cdot OH]_{ss}$), 20.0 μM nitrobenzene (NB) was employed to probe the radical concentration [24]. The observed decay rates referred to NB's disappearance through PMS and volatilization, respectively. The concentration of NB was measured by HPLC with a photodiode array detector (excitation wavelength 265 nm) (Agilent 1100 HPLC). The mobile phase consisted of 60% acetonitrile (v/v) and 40% H₂O (with 0.1% acetic acid, v/v) at a flow rate of 0.3 mL/min.

The reaction of NB with SO_4^{2-} was reported to be negligible compared with $\cdot OH$ [24,25]. Hence, the removal rate of NB can be expressed by the following equations:

$$\frac{d[NB]}{dt} = -k_{\cdot OH,NB}[NB][\cdot OH]_{ss} - k_{PMS}[NB] - k_{vol}[NB] \quad (1)$$

$$\ln \frac{NB_0}{NB} = (k_{\cdot OH,NB}[\cdot OH]_{ss} + k_{PMS} + k_{vol})t = k_{obs}t \quad (2)$$

$$[\cdot OH]_{ss} = \frac{k_{obs} - k_{PMS} - k_{vol}}{k_{\cdot OH,NB}} \quad (3)$$

where $k_{\cdot OH,NB}$ is the reaction rate constant between NB and $\cdot OH$, taken as $3.9 \times 10^9\text{ M}^{-1}\text{ s}^{-1}$. k_{PMS} and k_{vol} represent the observed first-order rate constants of NB's disappearance through PMS and volatilization, respectively. Furthermore, the atrazine degradation in kaolinite/PMS system can be expressed as follows:

$$\frac{d[ATZ]}{dt} = -k_{\cdot OH,ATZ}[ATZ][\cdot OH]_{ss} - k_{SO_4^{2-},ATZ}[ATZ][SO_4^{2-}]_{ss} - k_{PMS}[ATZ] \quad (4)$$

$$\ln \frac{ATZ_0}{ATZ} = (k_{\cdot OH,ATZ}[\cdot OH]_{ss} + k_{SO_4^{2-},ATZ}[SO_4^{2-}]_{ss} + k_{PMS})t = k_{obs}t \quad (5)$$

$$[SO_4^{2-}]_{ss} = \frac{k_{obs} - K_{PMS} - k_{\cdot OH,ATZ}[\cdot OH]_{ss}}{k_{SO_4^{2-},ATZ}} \quad (6)$$

where $k_{\cdot OH,ATZ}$ and $k_{SO_4^{2-},ATZ}$ are the reaction rate constants between atrazine and $\cdot OH$ or atrazine and SO_4^{2-} , respectively, taken as $3.5 \times 10^9\text{ M}^{-1}\text{ s}^{-1}$ and $2.7 \times 10^9\text{ M}^{-1}\text{ s}^{-1}$, respectively [26]. k_{PMS} represent the observed first-order rate constants of atrazine's disappearance through PMS. The other relevant data can be obtained from Fig. 7 and S9.

2.5. The reusability tests

The recycling tests were conducted to demonstrate the stability and reusability of kaolinite. Each cycle, the PMS and atrazine solution were replenished to make the initial reaction condition identical to the first cycle according to the residual PMS and atrazine content. Finally, the concentration of atrazine was measured by HPLC with the same method as shown in Text S1.

3. Results and discussion

3.1. Characterizations of fresh and used kaolinite

In this study, crystallographic and structural characteristics of kaolinite before and after reactions are presented in Fig. 1(b). The

diffraction spectra with specific peaks corresponding to (001), (020), (-111), ($-1-11$), (002), (-130), ($-1-31$), ($-1-13$), (-240), and (-331) can be assigned to the standard kaolinite pattern (JCPDS 78-1996) [19]. As shown in Table S1, there are no significant change for kaolinite after the degradation reaction including the peak position, crystal spacing, relative intensity and full width at half maxima (FWHM), indicating the stability of natural kaolinite after reaction [27,28]. FTIR was employed to explore the change in valence bonding and functional group of fresh and used kaolinite (Fig. 1c). Bands at 3620 and 3695 cm^{-1} could be attributed to the stretching of $-\text{OH}$ groups coordinated to the octahedral. Water bending band was also observed at around 1631 cm^{-1} . Bands at 1114, 1033 and 1010 cm^{-1} can be assigned to Si–O stretching modes, peak centered at 1010 cm^{-1} is caused by the vibration parallel to the layers (basal O_2^-), while the 1114 cm^{-1} band is due to a vibration perpendicular to the layers. Si–O (432 cm^{-1}), Si–O–Si in-plane bending (468 cm^{-1}), Si–O–Al bending (538 cm^{-1}), Si–O out-of-plane bending (696 cm^{-1}), and Al–Al–OH bonds (913 cm^{-1}) were clearly observed for both fresh and used kaolinite [27,29,30]. Compared to the fresh kaolinite, the FTIR spectra of the used kaolinite only shows a slight blue shift because the acidic condition might have changed the charge density of kaolinite [28]. As shown in Fig. 1(d) and (e), the surface area and pore volume increased a bit after reaction which could be attributed to the minor changes of kaolinite interlayers' spacing during the reaction [31].

The morphologies of fresh and used kaolinite are presented in Fig. 2. The kaolinite is one kind of mineral with basal and edge surfaces and plate-like structure. The fresh kaolinite is arranged in booklet agglomerates, with 0.5–1.0 μm in width. The morphology of used kaolinite kept stable after the reactions with PMS and atrazine as shown in Fig. 2(d–f). Kaolinite layers inside the bulk kaolinite still show hexagonal platelets without rolling or folding, demonstrating the strong stability of kaolinite in activating PMS.

XPS spectra were used to further investigate the surface characteristics and valence states of the fresh and used kaolinite (Figs. 3 and S8), and the percentages of the detected atomic constituents are shown in Table S2. High-resolution XPS spectra of Si 2p, Al 2p, and O 1s were presented for both fresh and used kaolinite after the peaks fitting. Binding energy at 103.0 eV can be attributed to the SiO_2 within the structure of kaolinite [32]. The peak at 74.6 eV can be assigned to the Al_2O_3 or AlO(OH) based on previous research studies [32,33]. The O 1s peak located at 532.1 eV can be deconvoluted into three components, which can be assigned to bridging OH (~531.5 eV), terminal OH

(~532.0 eV), and adsorbed H_2O (~532.7 eV) [34]. Comparing the O 1s spectra of fresh and used kaolinite shows that the bridging OH intensity decreased to some extent, indicating the bridging and terminal OH involved into the activation of PMS. There are no distinct peaks of S and Fe in the survey spectra which only occupied a small part of the samples (less than 0.5%). The iron in kaolinite is in the form of ferric oxide (Fe_2O_3) rather than ferrous oxide (FeO). It is difficult to activate the PMS through the Fe^{3+} alone in the degradation system [35], confirming the negligible role of Fe^{3+} in activating PMS. Overall, the binding energy position and the relative intensity of the peaks of Si 2p and Al 2p did not change significantly after reactions, while the peaks of O 1s changed after reactions, indicating the involvement of bridging and terminal OH in the activation of PMS.

3.2. Radicals analysis in kaolinite/PMS system

Hydroxyl, sulfate, sulfite and peroxyomonosulfate anion radicals are type of radicals generated in the process of PMS activation [26]. During a series of reactions between electrons (e^-) and adsorbed oxygen, hydroxyl radicals can be generated on the surface of kaolinite. Due to their low oxidation ability, the contributions of $\text{SO}_3^{\cdot-}$ ($E^0(\text{SO}_3^{\cdot-}) = 0.63 \text{ eV}$) and $\text{SO}_5^{\cdot-}$ ($E^0(\text{SO}_5^{\cdot-}) = 0.81 \text{ eV}$) to the degradation of atrazine might be negligible in the presence of $\text{SO}_4^{\cdot-}$ and $\cdot\text{OH}$. To identify the dominant oxidation species in the kaolinite/PMS system, radical quenching experiments were carried out using different concentrations of ethanol (EtOH) and tert-butyl alcohol (t-BuOH). Generally, alcohols like EtOH with α -hydrogen could scavenge both $\cdot\text{OH}$ and $\text{SO}_4^{\cdot-}$ rapidly, while t-BuOH without α -hydrogen can only quench $\cdot\text{OH}$. As shown in Fig. 4, the degradation efficiencies of atrazine decreased with the increase of EtOH or t-BuOH. However, 100 mM EtOH could completely inhibit the decomposition of atrazine by kaolinite/PMS, while about 30% of atrazine could be degraded in the presence of 100 mM t-BuOH at 120 min. The results indicated that both $\cdot\text{OH}$ and $\text{SO}_4^{\cdot-}$ contributed to the degradation of atrazine in the kaolinite/PMS process.

EPR analysis was conducted to further confirm the generation of $\text{SO}_4^{\cdot-}$ and $\cdot\text{OH}$ using DMPO as the probe compound. As shown in Fig. 5(a), no characteristic signals were presented with PMS alone after adding DMPO as the probe, indicating the stability of PMS without outer excitation. In Fig. 5(b), for the kaolinite/PMS reaction, the characteristic signals of DMPO-OH (with the intensities of 1:2:2:1) and DMPO- $\text{SO}_4^{\cdot-}$ signal peaks (weaker peaks between hydroxyl radicals)

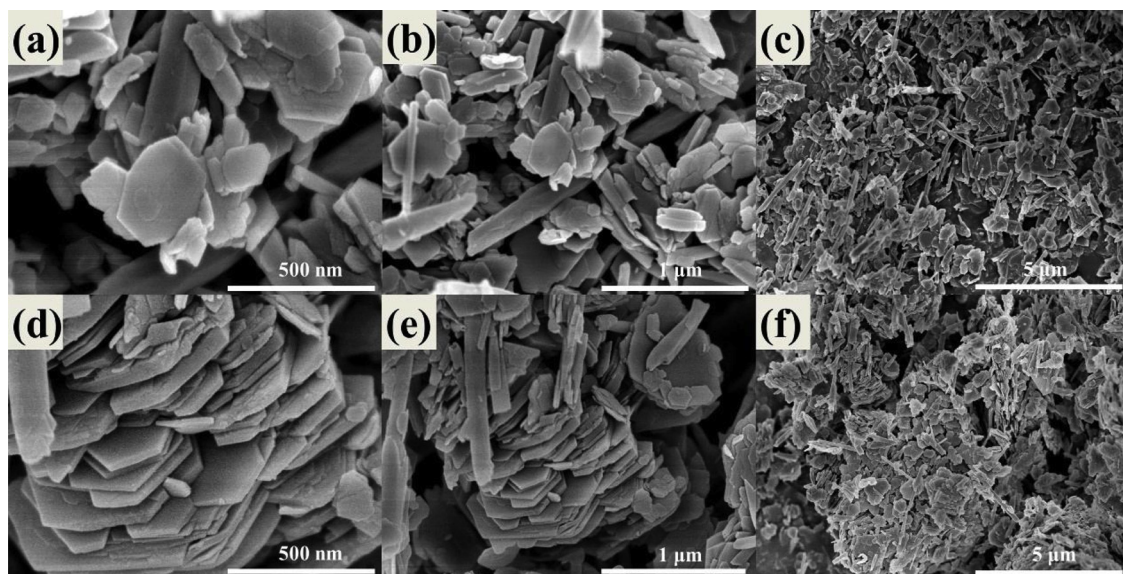


Fig. 2. FESEM images of fresh kaolinite (a–c) and used kaolinite (d–f).

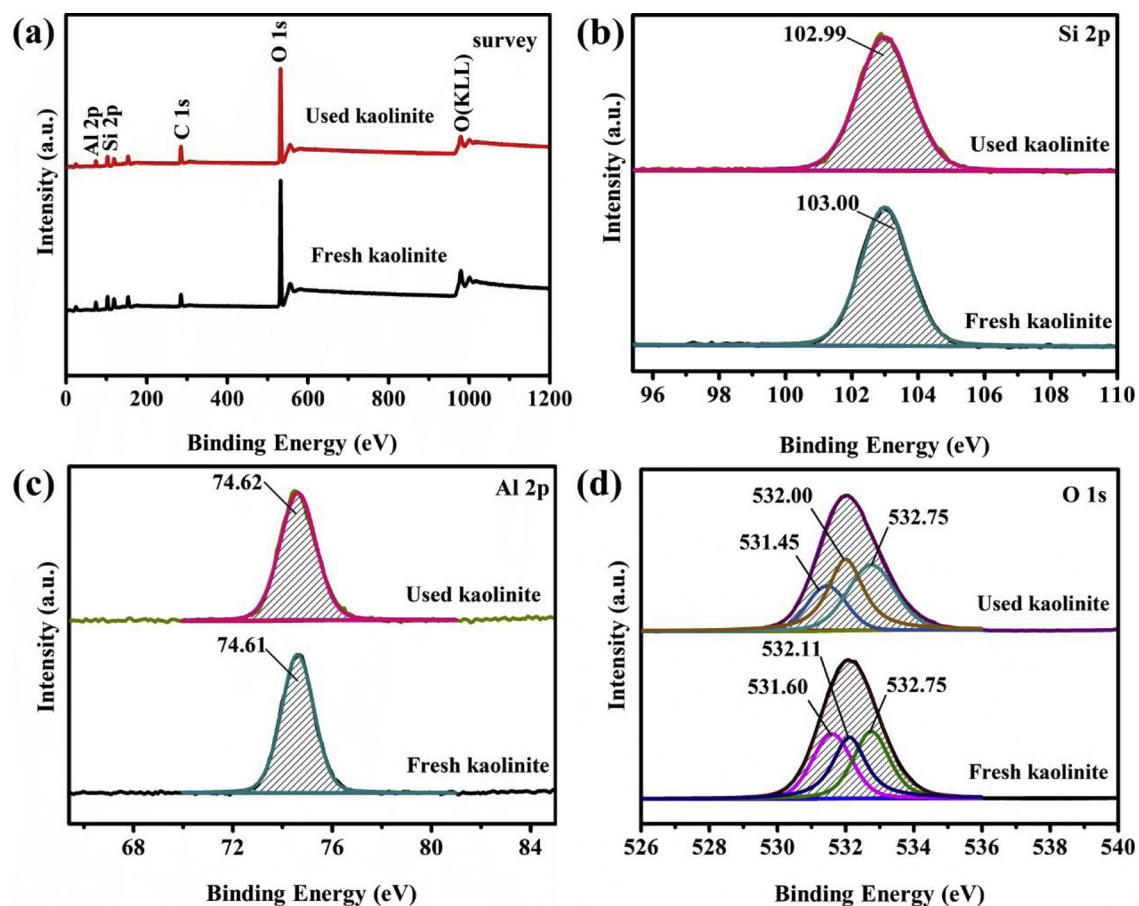


Fig. 3. XPS spectra of survey, Si 2p, Al 2p and O 1s for fresh and used kaolinite.

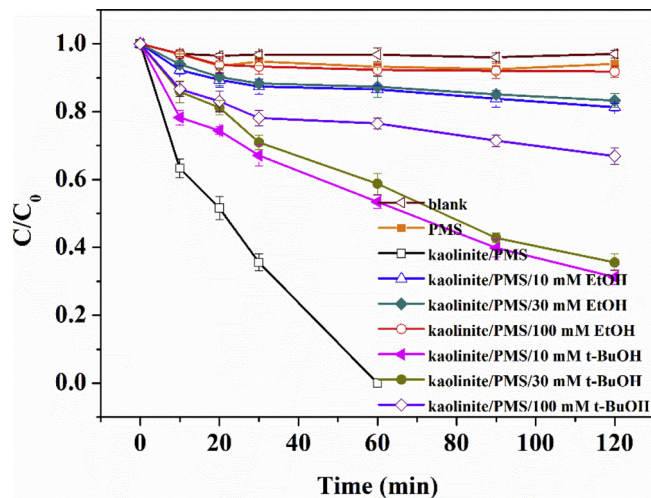


Fig. 4. Effects of radical scavengers (EtOH and t-BuOH) towards the degradation system. Generation condition: C_0 (atrazine) = 4.6 μ M, C_0 (catalyst) = 1.0 g/L, C_0 (PMS) = 1.0 mM, V = 30 mL, initial pH = 3.4, temperature = 293 K.

were found in the EPR spectra at 10 min and 20 min, respectively, suggesting that natural kaolinite could activate PMS to produce $\text{SO}_4^{\cdot-}$ [36]. It is interesting that when the DMPO was added into kaolinite/PMS system at the beginning of the reaction, the intensity of the signals of $\cdot\text{OH}$ and $\text{SO}_4^{\cdot-}$ increased significantly even at 10 min (Fig. 5(c)). However, the signal of $\text{SO}_4^{\cdot-}$ was not observed, while a new signal (DMPOX) was produced and became much strong at 20 min. The nitroxide radical peak (DMPOX) was due to the direct oxidation by single electron rather than the spin-trapping of DMPO-OH [37]. Amounts of

$\cdot\text{OH}$ generated by H_2O_2 through hydrolyzing HSO_5^- would oxidize the spin trapping agent to DMPOX in the absence of degradation pollutant, atrazine [38]. Furthermore, the free radicals generated during the PMS/kaolinite/atrazine process were monitored along with the reaction time (Fig. 5(d)). The intensities of DMPO-OH and DMPO-SO₄ were gradually enhanced with the time, suggesting the presence of both $\cdot\text{OH}$ and $\text{SO}_4^{\cdot-}$ in the degradation process of atrazine by kaolinite/PMS.

3.3. Effects of catalyst dosage, pH, PMS dosage, and atrazine concentration

In this work, atrazine was used as the target pollutant to test the catalytic ability of kaolinite towards PMS with optimized reaction parameters (Fig. 6), and the final pH after reactions can be found in Fig. S1. As shown in Fig. 6(a), the removal efficiency of atrazine by either PMS or kaolinite was extremely low at current reaction conditions. The degradation efficiency dramatically increases when using both PMS and kaolinite. The increase in kaolinite dosage resulted in an increase in the degradation rates of atrazine. When the kaolinite dosage increased to 1.0 g/L, the degradation extent of atrazine exceeded 90% at 60 min.

The effect of initial pH on the degradation of atrazine was investigated due to the important role of pH in affecting the surface potential of kaolinite and the PMS activation processes (Fig. 6(b)). Different initial pH values were chosen in the range of 1.5–12.5. It is noticed that the degradation rate of atrazine increased in the pH range of 3 to 11, while decreased dramatically when the pH was lower than 3 or higher than 11. Firstly, the active sites on the surface of kaolinite can be influenced by the concentration of H^+ or OH^- in the reaction matrix. The zeta potential of kaolinite is around 2.65 as shown in Fig. S2. Excess H^+ or OH^- could affect the presence of surface-bonded and structural hydroxyl groups significantly [11,39]. Secondly, both $\cdot\text{OH}$

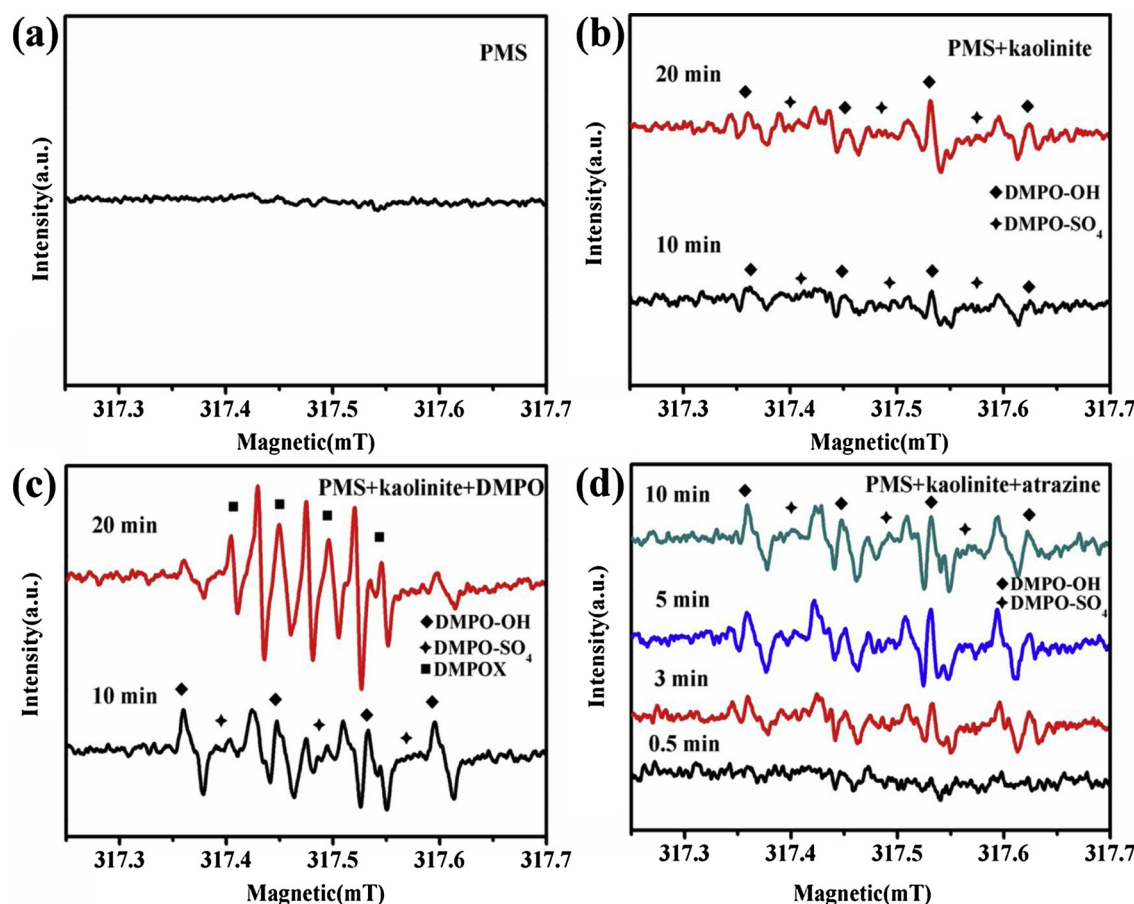


Fig. 5. Electron spinning resonance (ESR) spectra of (a) pure PMS in aqueous solution; (b) kaolinite/PMS system with reaction time of 10 min and 20 min; (c) PMS/kaolinite/DMPO system with reaction time of 10 min and 20 min; (d) PMS/kaolinite/atrazine system with reaction time of 0.5 min, 3 min, 5 min, and 10 min. General condition: PMS = 100 mM (a, b and c) or 10 mM (d), kaolinite = 1.0 g/L, DMPO = 5 mM, atrazine = 4.6 μ M.

(1.8–2.7 V) and $\text{SO}_4^{\cdot-}$ (2.5–3.1 V) can be significantly affected by the solution pH. At low pH ($\text{pH} < 3$), H^+ can scavenge sulfate radical ($\text{SO}_4^{\cdot-}$) resulting in a decrease in the degradation rate of atrazine. As pH increases at values higher than 3, $\text{SO}_5^{\cdot-}$ can be decomposed into $\text{SO}_4^{\cdot-}$, which can subsequently react with OH^- to form $\cdot\text{OH}$ at higher pH ($7 < \text{pH} < 11$) [40]. As for the dramatic drop under strong alkaline condition ($\text{pH} > 11$), this was because abundant SO_5^{2-} would be generated from PMS, preventing the generation of $\text{SO}_4^{\cdot-}$ and $\cdot\text{OH}$ in the reaction system [40]. Thus, the optimum performance was observed from weak acid to weak alkaline environment (i.e., $4 < \text{pH} < 11$), whose pH range is wider than in the case of previous reports [41,42].

Fig. 6(c) shows that atrazine degradation by kaolinite/PMS is dependent on the PMS dosage. The atrazine degradation rate increased when PMS was increased in the range of 0–1.0 mM but decreased when the PMS was increased from 1.0 mM to 5.0 mM, suggesting 1.0 mM as an optimum PMS dosage for achieving the highest atrazine degradation rate in the kaolinite/PMS system. Although more PMS could produce more oxidant species, the excess PMS would compete with target compounds for the reactive species [43]. Hence, the follow up experiments were conducted with 1.0 mM PMS based on the degradation results.

Effect of initial pollutant concentration in the degradation process on the degradation of atrazine by kaolinite/PMS was explored as well. As displayed in Fig. 6(d), the degradation percentage was gradually decreased with the increase of initial atrazine concentration. Nevertheless, even 90% of atrazine can be removed at an initial concentration of 5 mg/L, suggesting kaolinite is an efficient catalyst for PMS activation.

3.4. Effects of inorganic ions and NOM

Inorganic anions, such as Cl^- , NO_3^- , HCO_3^- and H_2PO_4^- , are widely presented at various concentrations in real wastewaters, reacting with the reactive species (i.e., $\text{SO}_4^{\cdot-}$ and $\cdot\text{OH}$) and affecting the catalytic reactions [12]. H_2PO_4^- usually shows inhibition effect on the PMS heterogeneous activation processes [44,45], however, it accelerated the degradation of atrazine by kaolinite/PMS as shown in Fig. 7(a). To gain an insight into the positive effect of H_2PO_4^- on kaolinite/PMS process, nitrobenzene (NB) was used to calculate the steady-state concentration of $\text{SO}_4^{\cdot-}$ and $\cdot\text{OH}$ ($[\text{SO}_4^{\cdot-}]_{\text{ss}}$ and $[\cdot\text{OH}]_{\text{ss}}$) in the kaolinite/PMS/ H_2PO_4^- system. The detailed results can be found in Fig. S9. The steady-state concentrations of $\text{SO}_4^{\cdot-}$ and $\cdot\text{OH}$ were enhanced with the increase of H_2PO_4^- concentration from 0 to 10 mM (Fig. 7(b)). Besides, as shown in Fig. 7(c–f), the contributions of PMS, $\text{SO}_4^{\cdot-}$ and $\cdot\text{OH}$ to the time-dependent degradation of atrazine by kaolinite/PMS were calculated in the presence of H_2PO_4^- at different concentrations (0–10 mM). PMS alone did not contribute a significant role in degrading atrazine considering the small reaction rate. The removal of atrazine due to $\cdot\text{OH}$ -oxidation enlarged as the H_2PO_4^- concentration increased. $\text{SO}_4^{\cdot-}$ -oxidation contributed to the largest removal portion of atrazine in kaolinite/PMS. Moreover, the residual PMS decreased as the concentration of H_2PO_4^- increased (Fig. S10), indicating H_2PO_4^- was beneficial for the decomposition of PMS. The asymmetric structure of PMS makes it easily attacked by nucleophiles [46] such as H_2PO_4^- and decomposed quickly, leading to more reactive species, including $\cdot\text{OH}$ and $\text{SO}_4^{\cdot-}$, for the degradation of atrazine.

It is necessary to analyze the effect of Cl^- , which is extensively distributed in effluents of tannery, dye manufacturing and oil extraction

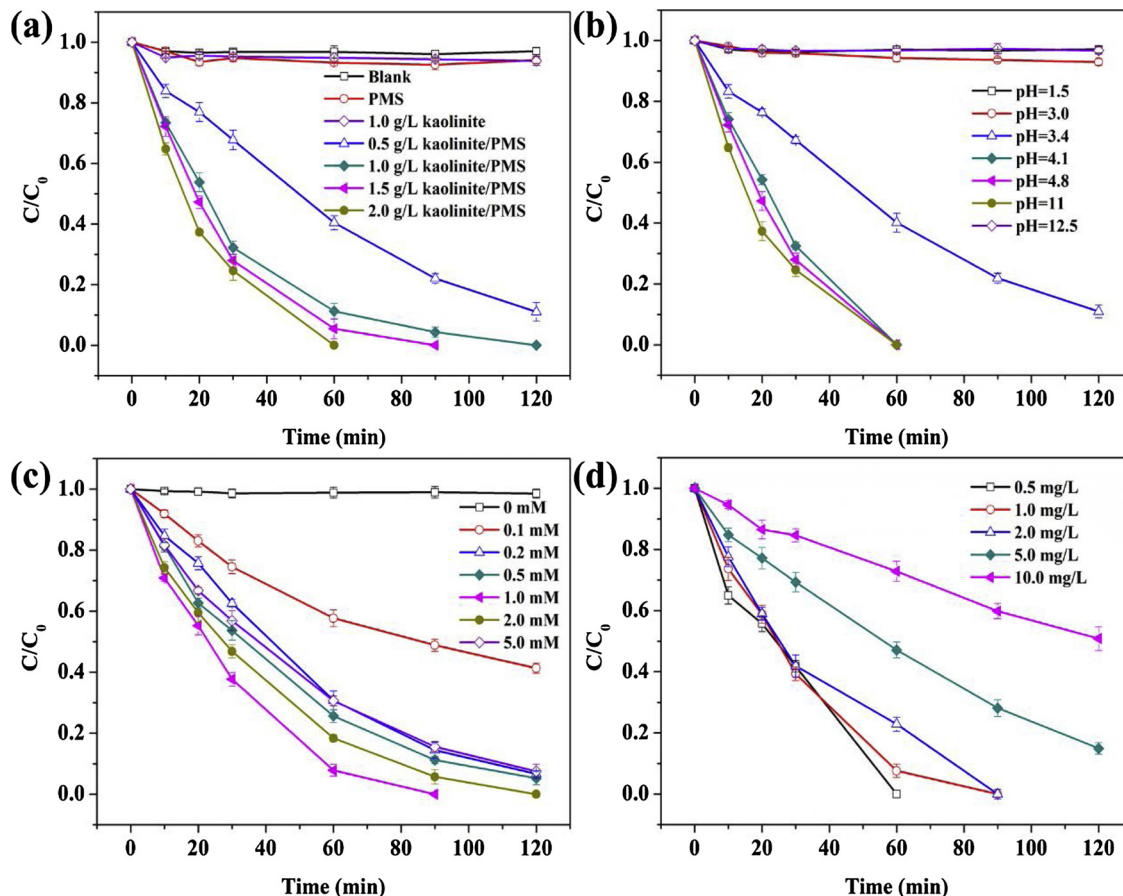


Fig. 6. Effects of catalyst loading (a), initial pH (b), PMS dosages (c), and initial atrazine concentration (d) on the atrazine degradation in kaolinite/PMS system. General conditions: C_0 (atrazine) = 4.6 μM , C_0 (catalyst) = 1.0 g/L, C_0 (PMS) = 1.0 mM, V = 30 mL, initial pH = 3.4, temperature = 293 K.

wastewater. Fig. 8(a) depicts the suppression effect of Cl^- on the degradation of atrazine by kaolinite/PMS. This was mainly caused by the reactions of chloride ions with $\cdot\text{OH}$ and $\text{SO}_4^{\cdot-}$, resulting in the formation of secondary chlorine radicals such as $\cdot\text{Cl}$, $\cdot\text{Cl}_2^-$ and $\cdot\text{ClO}\text{H}^-$ with lower redox potentials [41]. In the presence of NO_3^- , significant reduction in degradation rate of atrazine was also observed because NO_3^- can rapidly react with $\text{SO}_4^{\cdot-}$ to form NO_3^{\cdot} at a high rate as $8.8 \times 10^8 \text{ M}^{-1} \text{ s}^{-1}$ [45]. The degradation of atrazine only shows a slight decline when adding HCO_3^- (2 mM) in kaolinite/PMS. When the HCO_3^- concentration increased to 5 mM, the degradation efficiency of atrazine significantly decreased as only 50.0% atrazine was decomposed within 60 min. This is because HCO_3^- can react with $\text{SO}_4^{\cdot-}$ and $\cdot\text{OH}$ to generate carbonate radical ($\text{CO}_3^{\cdot-}$), which has lower oxidation ability towards atrazine [47,48].

NOM as radical scavengers can react with $\text{SO}_4^{\cdot-}$ and $\cdot\text{OH}$ rapidly due to the carboxyl groups and phenolic hydroxyls [49]. As shown in Fig. 8(b), atrazine degradation was inhibited with the addition of NOM (0.2–10 mg/L). The degradation of atrazine decreased to 50.0% when the NOM concentration increased to 10.0 mg/L, indicating the detrimental role of NOM in the degradation process.

3.5. Reusability and TOC

The reusability and stability of catalysts are pivotal for application in wastewater treatment. As shown in Figs. 9 and S11, the kaolinite could be continuously used to catalyze PMS for the degradation of atrazine at high efficiency without general recycle procedures such as filtration, washing, and drying. The results showed that the kaolinite has a good reusability after four cycles. The residual TOC was also measured with an initial atrazine concentration of 5 mg/L to test the

mineralization efficiency of kaolinite/PMS process. As displayed in Fig. 9(b), both atrazine concentration and TOC decreased with time, and the final TOC removal efficiency was near 50%, much higher than the mineralization efficiency of other PMS related-AOPs [50,51]. This indicated that the mineralization efficiency of PMS related-AOPs could be significantly improved by activation of kaolinite. The effect of PMS dose on the mineralization of atrazine was investigated as well; the mineralization efficiency increased significantly first, and then maintained at around 60% due to the scavenging effects of PMS for reactive oxygen species and other radicals.

3.6. Transformation products analysis

To elucidate the transformation pathways of atrazine in the kaolinite/PMS system, Q-TOF-LC/MS was employed to determine the transformation products during the destruction of atrazine. The molecular structures of the transformation products were proposed and listed in Table S3 according to the observed mass-to-charge ratio (m/z). The evolution of the transformation products with time can be found in Figs. S6 and S7 and Table S4. It is noticed that the oxidation processes of atrazine were focused on the side chains (Fig. 10). Dealkylation, alkylidic-hydroxylation and alkylidic-oxidation reactions are the main routes to decompose atrazine [26]. For $\text{SO}_4^{\cdot-}$ initiated oxidation processes on atrazine, a N (exocyclic)-centered radical would be formed firstly through electron transfer, which could transfer to C-centered radicals via 1,2-H shift [26]. The C-centered radicals are readily attacked by dissolved O_2 to form peroxide radical, which subsequently transforms into double-bond derivatives (such as P214 and P4) with the removal of a per-hydroxyl radical. The double-bond derivatives would be oxidized into dealkylation products, i.e., P2, P3, P5, P7, P10, P11,

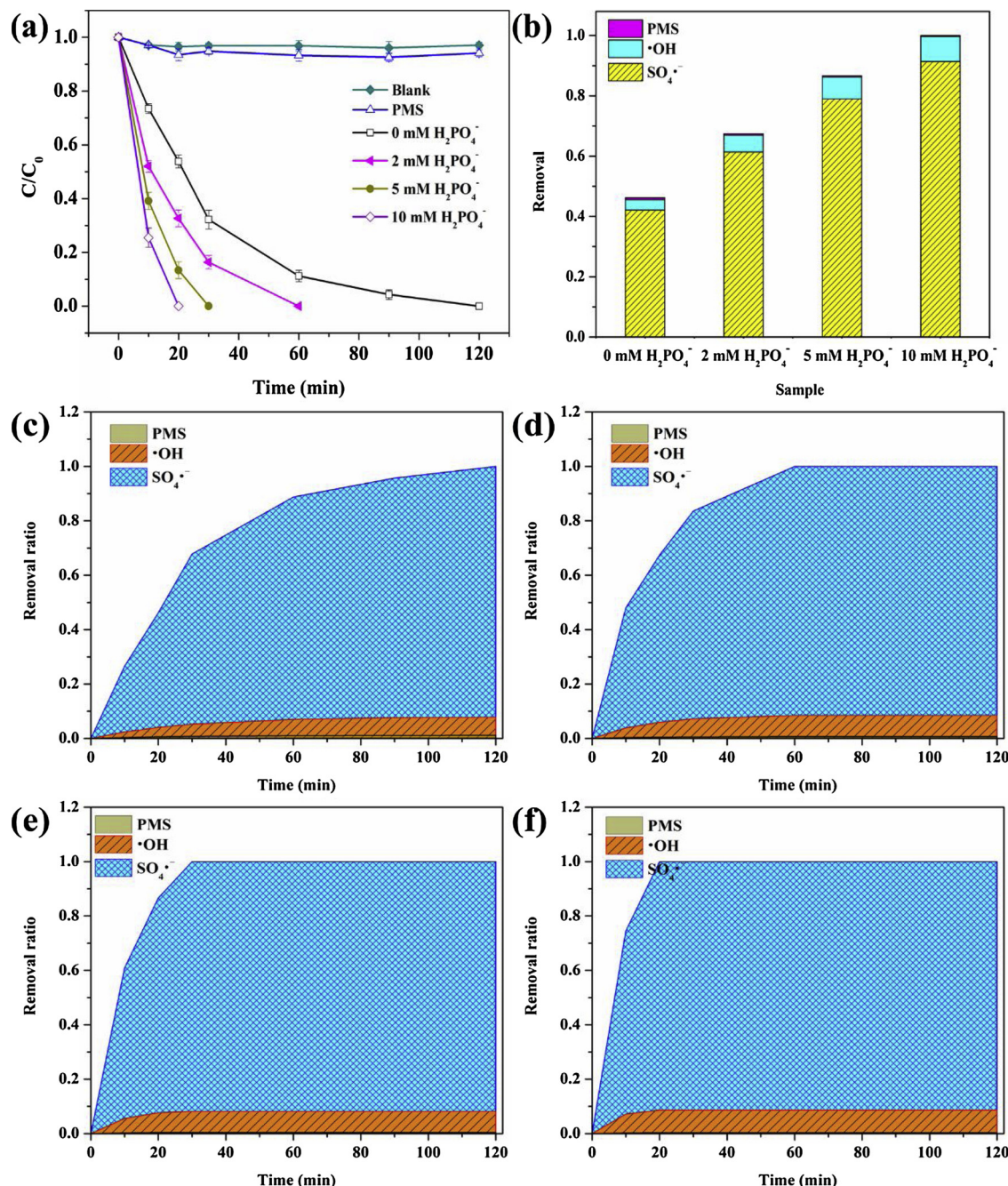


Fig. 7. (a) Effect of inorganic anion (H_2PO_4^-) (b) Removal of atrazine by PMS, $\text{SO}_4^{\cdot-}$ and $\cdot\text{OH}$ with the addition of H_2PO_4^- at different concentrations after 20 min; (c–f) Removal percentages of atrazine by PMS, $\text{SO}_4^{\cdot-}$ and $\cdot\text{OH}$ in the presence of 0 mM, 2 mM, 5 mM and 10 mM H_2PO_4^- , respectively. General conditions: C_0 (atrazine) = 4.6 μM , C_0 (catalyst) = 1.0 g/L, C_0 (PMS) = 1.0 mM, V = 30 mL, initial pH = 3.4, temperature = 293 K.

and P12. The continuous $\cdot\text{OH}$ attack on the C-centered radicals leads to the generation of alkylidic-hydroxylation products (P232 and P9), which further oxidized into imine products (P1, P2, and P10). The dechlorination-hydroxylation products were observed during the decomposition of atrazine, namely P9, P10, P11, and P12. The C–Cl bond within atrazine molecule is easy to be broken due to the relatively low bond polarity (0.293) and longest bond (1.734 Å) [52]. The C on which the chlorine atom is attached would be oxidized by $\text{SO}_4^{\cdot-}$ and H_2O to first form a $-\text{OH}$ adduct, which is then followed by a heterolytic cleavage of C–Cl bond to generate dechlorinated-hydroxylated derivatives.

3.7. Catalysis mechanisms

The compositions of fresh and used kaolinite in oxide form and single element form were detected by X-ray fluorescence spectroscopy (XRF) as shown in Table S5 and S6. The major elements of kaolinite were O, Si and Al, which account for 99% of the overall composition. As for other impurity elements, Fe has the highest content as around 0.50% in natural kaolinite and decreased to around 0.36% after the reaction. To exclude the possible contribution of Fe^{3+} to PMS activation, Fe^{3+} (10 mg/L)/PMS was employed and found that less than 10% of atrazine at 120 min was degraded (Fig. S4), where the dose of Fe was much higher than that leached in the reaction solutions under kaolinite/PMS system (10.08 $\mu\text{g}/\text{L}$). Furthermore, other impurity elements

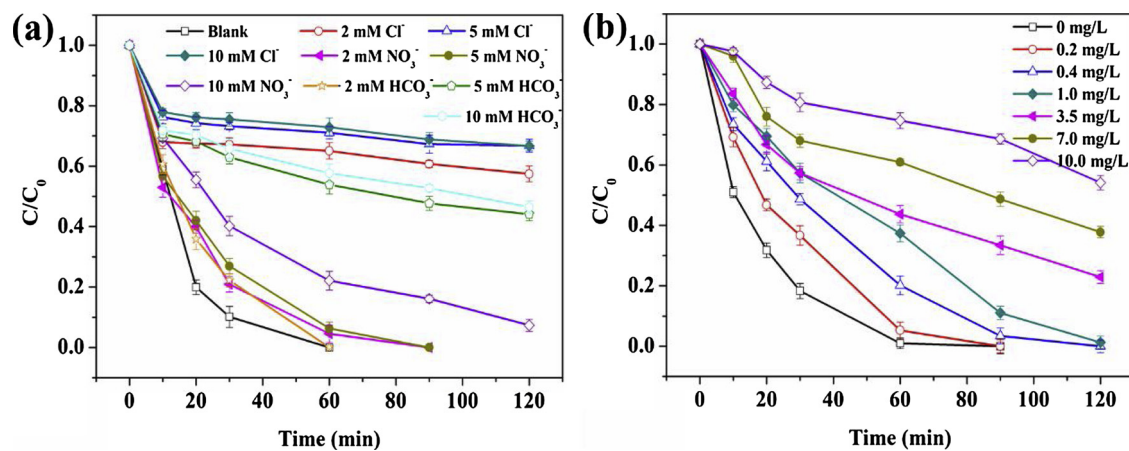


Fig. 8. Effects of (a) inorganic anions (Cl^- , NO_3^- and HCO_3^-), (b) NOM concentration, general conditions: C_0 (atrazine) = 4.6 μM , C_0 (catalyst) = 1.0 g/L, C_0 (PMS) = 1.0 mM, V = 30 mL, initial pH = 3.4, temperature = 293 K.

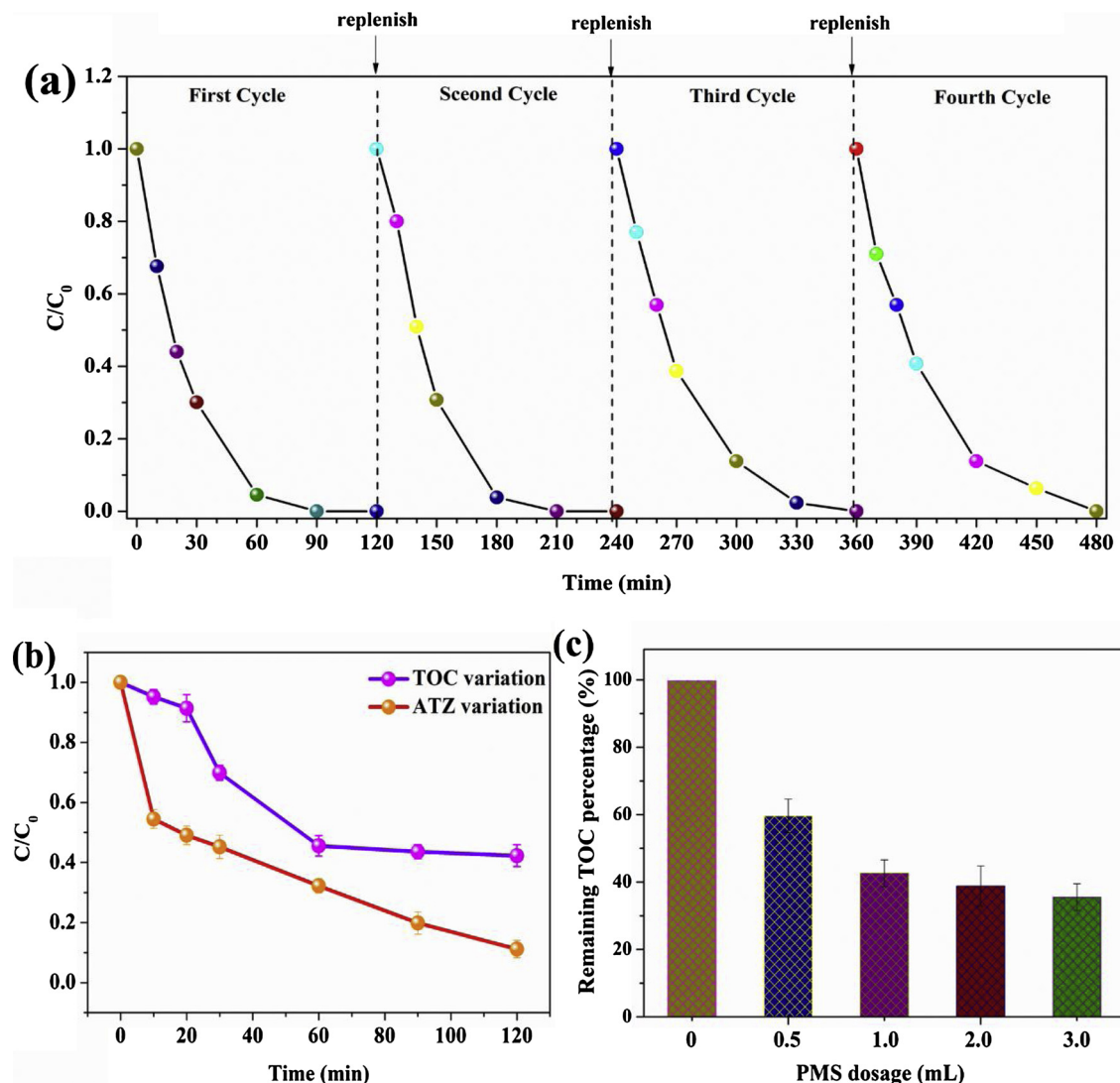
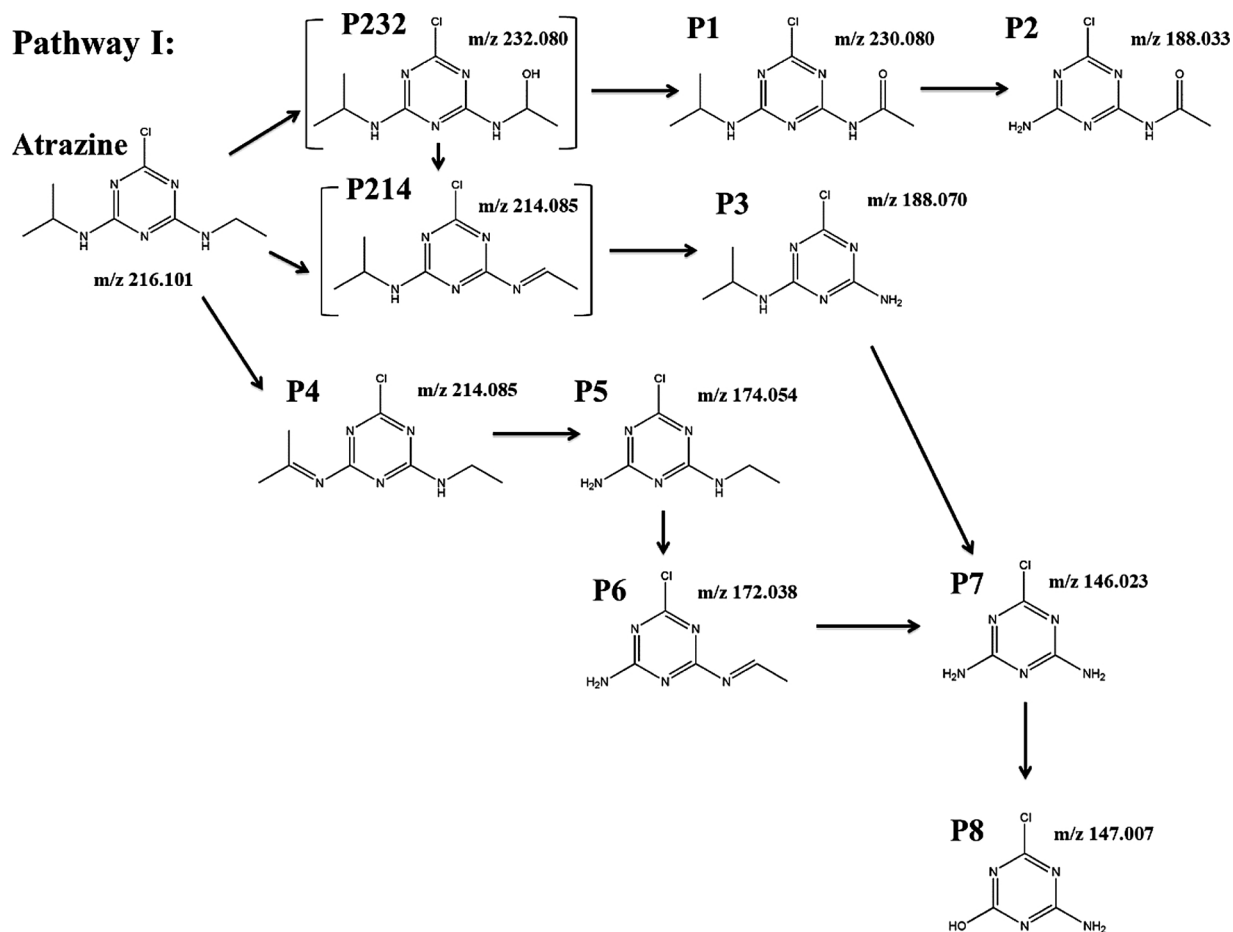


Fig. 9. (a) The reusability experiments of kaolinite. General conditions: C_0 (atrazine) = 4.6 μM , C_0 (PMS) = 1.0 mM, C_0 (catalyst) = 1.0 g/L, initial pH = 3.4, V = 30 mL, temperature = 293 K. (b) The total organic carbon (TOC) variation with time, (c) remaining TOC percentage with the increase of PMS dosages. General conditions: C_0 (atrazine) = 23 μM , C_0 (PMS) = 1.0 mM, C_0 (catalyst) = 2.0 g/L, initial pH = 3.4, V = 30 mL, temperature = 293 K.



Pathway II:

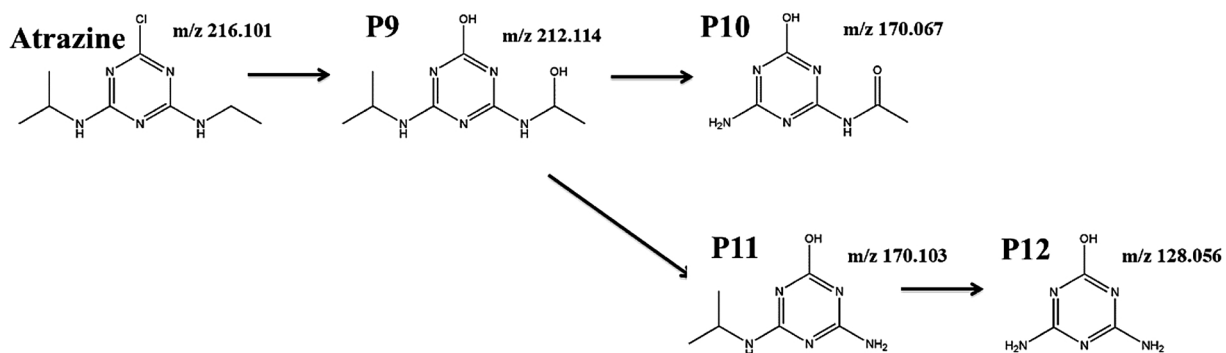


Fig. 10. Possible degradation pathways of atrazine.

had lower contents and fluctuated slightly as seen from Table S5, the leaching concentration of Al^{3+} , Fe^{3+} and Zn^{2+} were measured by ICP-MS as 89.96 $\mu\text{g/L}$, 10.08 $\mu\text{g/L}$ and 35.78 $\mu\text{g/L}$, respectively (Table S7), indicating the negligible effect of metal ions towards the degradation system [35]. The results in Fig. S5 further proved that Al^{3+} cannot be used to activate PMS.

Based on the XPS spectra and the unique “TO” structure of kaolinite, it is inferred that the catalytic ability of kaolinite for the PMS activation was mainly due to the rich OH groups embedded into the inner or external surface. To demonstrate the hypothesis, kaolinite was calcinated at different temperature and the functional groups of kaolinite were further characterized by FTIR as shown in Fig. 11. For the kaolinite calcined at 900 °C, the intensity of the adsorption band at 468.78 and

1095.97 cm^{-1} could be attributed to Si—O—Si vibration while the band at 811.31 cm^{-1} could be assigned to Al—O—Al vibration, indicating that the main skeleton was still composed of silicon and aluminum oxides [39]. Nevertheless, compared with the sample calcined at 900 °C, the sample calcined at 200 °C showed similar spectra to those of fresh kaolinite. However, bands at near 3620 and 3695 cm^{-1} assigned to the stretching of OH groups coordinated to the octahedral, water bending band observed at around 1631 cm^{-1} , and Al—Al—OH bonds at near 913 cm^{-1} disappeared after the calcination. The change of surface-bonded and structural hydroxyl groups on kaolinite with temperature increase can also be demonstrated by the NH_3 -TPD result (Fig. 12(b)). It is reported that kaolinite almost has no acidity, nevertheless, the intensity increased gradually with temperature (especially

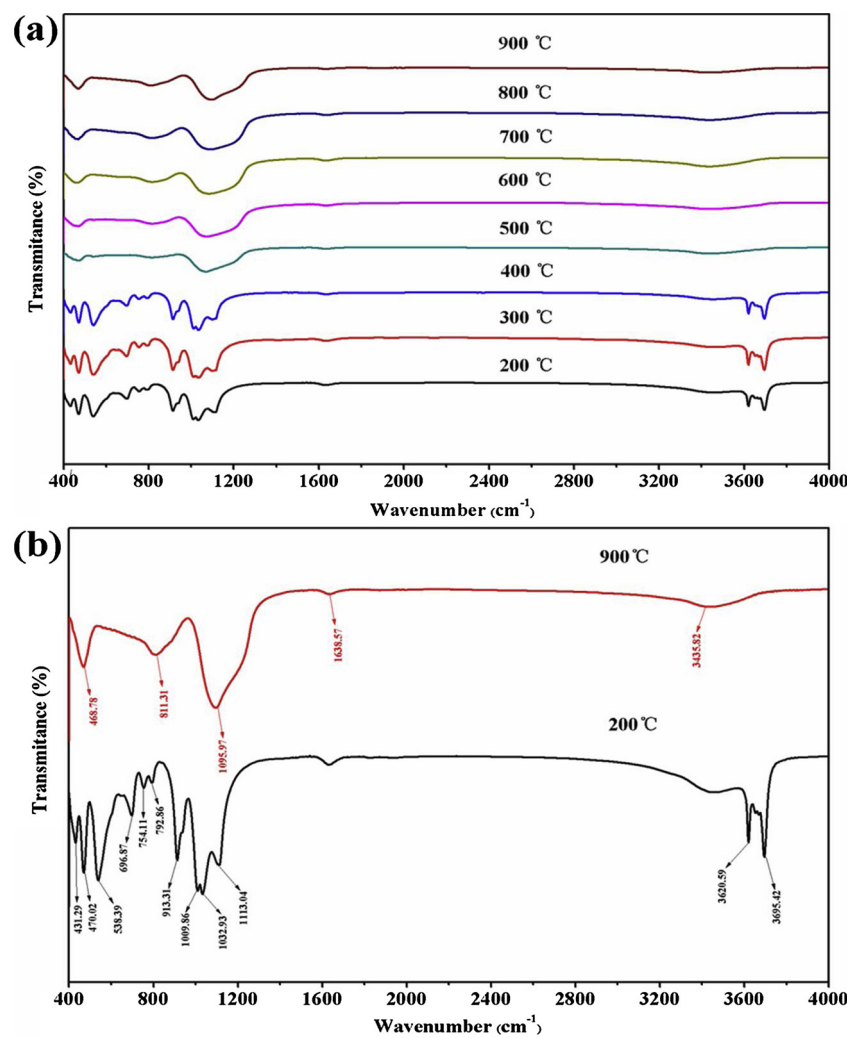


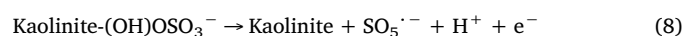
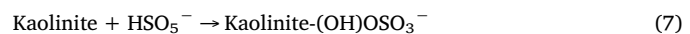
Fig. 11. (a) FTIR spectra for kaolinite with different calcination temperature, (b) the specific FTIR spectra for kaolinite calcined at 200 °C and 900 °C.

after 400 °C), indicating the removal of surface-bonded and structural hydroxyl groups on kaolinite [53]. The kaolinite calcined at different temperature was used to catalyze PMS for decomposing atrazine (Fig. 12(a)). The degradation of atrazine decreased dramatically with increase in calcination temperature, indicating that the hydroxyl groups on the surface and within the interlayers play a dominant role in activating PMS to generate reactive species, such as ·OH and SO₄²⁻. Previous literature studies also proved that more OH groups could increase the electron density and act as σ-donor ligands which lower the redox activation energy and increase the PMS activation reaction. Furthermore, the electron mediation process also increases due to the effective linkage of OH⁻ and redox partners by bridged-surface ligand [54].

Additionally, different natural minerals were applied to activate PMS and the theoretical formulas can be found in Table S8. Fig. 12(c) showed that different natural minerals had different degradation efficiency under the same reaction conditions, which might be ascribed to the surface-bonded and structural hydroxyl group of the catalysts. Natural minerals without surface-bonded and structural hydroxyl group (diatomite, zeolite) displayed no degradation. Natural minerals with a small amount of surface-bonded and structural hydroxyl group (illite, montmorillonite) displayed around 20% removal after 120 min. The palygorskite (around 35% removal) and sepiolite (around 50% removal) have a moderate amount of surface-bonded and structural hydroxyl group. Kaolinite with the most abundant surface-bonded and structural hydroxyl groups displayed the best degradation efficiency (100%), demonstrating the decisive role of surface-bonded and

structural hydroxyl groups in activating PMS.

The FTIR spectra for PMS, kaolinite and kaolinite/PMS in water matrix were explored to investigate the interaction between kaolinite and PMS. As seen from Fig. 12(d), for the PMS only, the wavelength at about 1634 cm⁻¹ and 3364 cm⁻¹ could be ascribed to the peaks of pure water [55], and bands at around 1102 cm⁻¹ and 1247 cm⁻¹ are attributed to S – O stretching vibration of either HSO₅⁻ or SO₄²⁻ [56]. The intensity of the 1247 cm⁻¹ and 1102 cm⁻¹ bands were obviously reduced in the presence of kaolinite. In addition, red-shifts of 9 and 14 cm⁻¹ were displayed compared with PMS alone, respectively. The result indicated that the OH in HSO₅⁻ has lower electron density when bonded to kaolinite surface and the kaolinite surface electrons donate electron to the OH of HSO₅⁻ which could inhibit the electron attraction from the neighboring S – O [56]. Furthermore, the band intensities at near 909, 1010, 3618 and 3690 cm⁻¹ ascribed to the stretching of OH groups were greatly enhanced compared with those of PMS. It is assumed that electron transfer takes place inside the surface of kaolinite-(OH)OSO₃⁻ complex, thus more new –OH groups can be formed, leading to the subsequent generation of sulfate radical [56]. The FTIR results proved that the PMS molecules were decomposed after chemically bonded to the surface of kaolinite with the formation of kaolinite-(OH)OSO₃⁻ complex. The mechanism diagram was shown in Scheme 1.



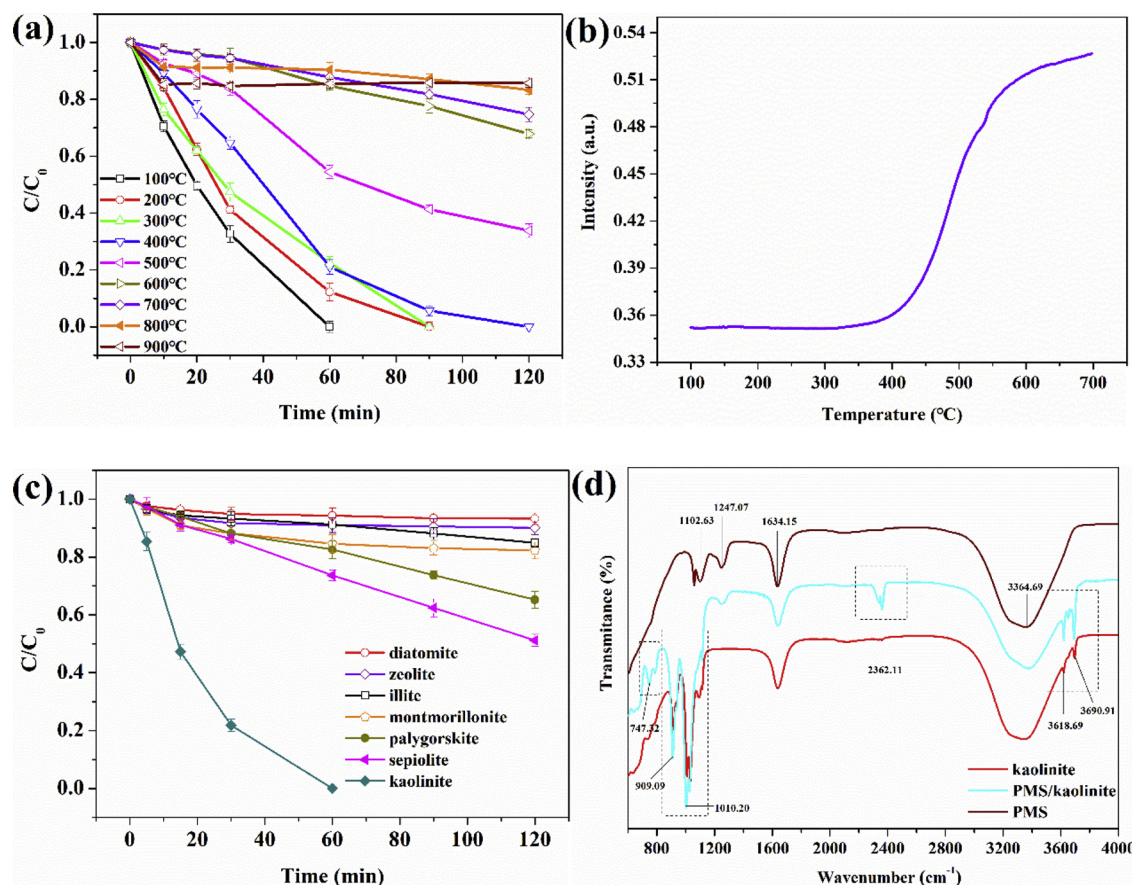
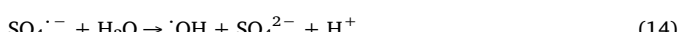
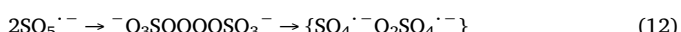
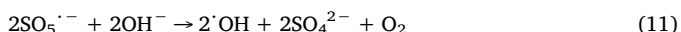


Fig. 12. (a) The degradation efficiencies of kaolinite subjected to different calcination temperatures. Reaction conditions: C_0 (atrazine) = 4.6 μ M, C_0 (catalyst) = 1.0 g/L, C_0 (PMS) = 1.0 mM, V = 30 mL, initial pH = 3.4, temperature = 293 K. (b) NH_3 -TPD result of kaolinite, (c) The degradation efficiencies of different natural minerals. Reaction conditions: C_0 (atrazine) = 4.6 μ M, C_0 (catalyst) = 1.0 g/L, C_0 (PMS) = 1.0 mM, V = 30 mL, initial pH = 3.4, temperature = 293 K. (d) FTIR spectra for kaolinite, PMS and kaolinite/PMS in water matrix.



Based on the discussion of XPS and ESR results, the activation mechanism of PMS by kaolinite can be proposed as Eqs. (7)–(15) [57,58]. Firstly, HSO_5^- was attached to the kaolinite via chemical bonds with the surface-bonded and structural hydroxyl groups. Secondly, electron transfer inside the kaolinite-(OH) OSO_3^- complex leads to the generation of SO_5^{2-} via loss of one electron. The generated electron could react with HSO_5^- to subsequently form SO_4^{2-} and $\cdot OH$. Additionally, SO_5^{2-} can transform to SO_4^{2-} or $S_2O_8^{2-}$ via self-combination as well. It is worth to mention that SO_4^{2-} and $\cdot OH$ can be converted through the degradation process as well. Finally, SO_4^{2-} and $\cdot OH$ can attack the side chains of atrazine with the formation of transformation products on the surface of kaolinite.

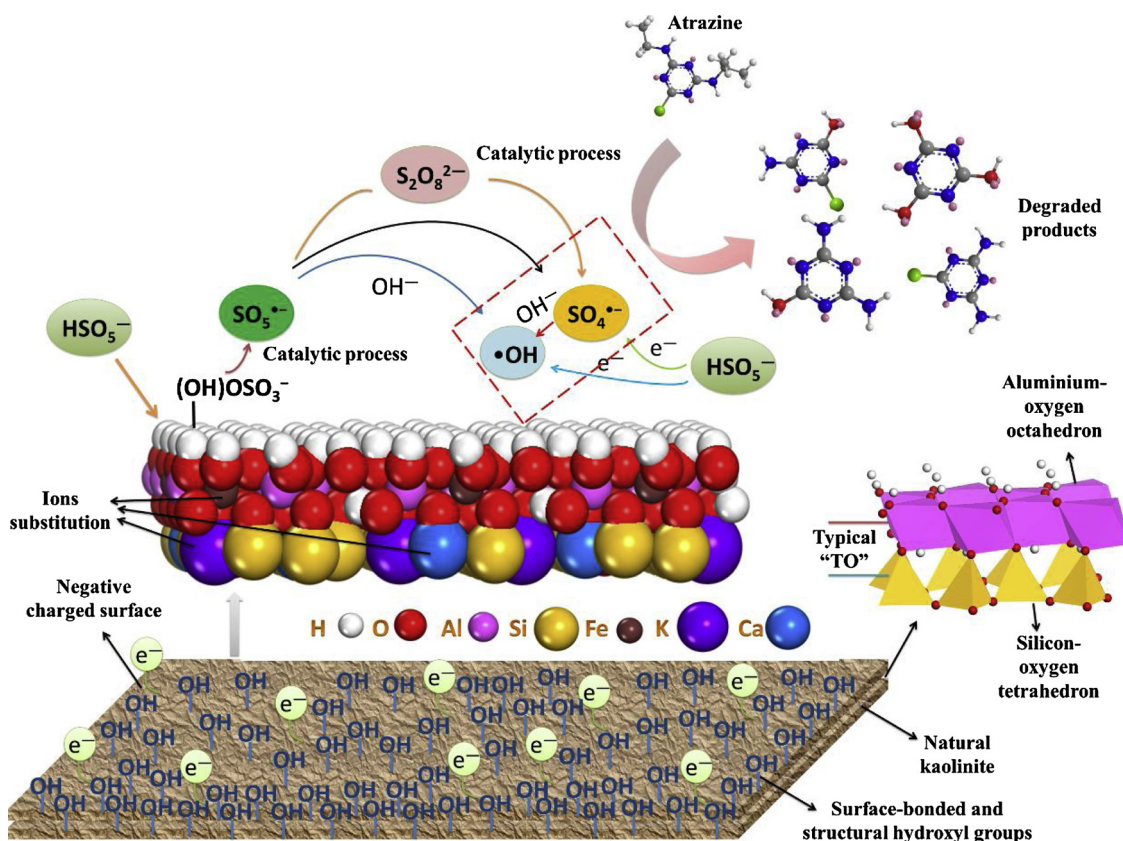
4. Conclusions

In summary, natural kaolinite was utilized to catalyze PMS for the efficient decomposition of atrazine for the first time. Results demonstrated the good catalytic ability of natural kaolinite for PMS activation.

The optimum reaction pH was between weak acid and weak alkaline environment (i.e., $4 < pH < 11$), and kaolinite/PMS could achieve a relatively high degree of mineralization. Cl^- , NO_3^- , and HCO_3^- decreased the degradation rates of atrazine in the kaolinite/PMS process, while $H_2PO_4^-$ improved the removal of atrazine. The possible degradation pathway of atrazine was also elucidated based on the results of Q-TOF-LC-MS. The material crystallinity, porosity structure, surface morphology, functional groups, and valence state of specific elements were well characterized. ESR and radicals scavenging experiments were also carried out to gain further insights of the catalysis mechanism for kaolinite/PMS. The results suggest that the surface-bonded and structural hydroxyl groups accounted as active sites for catalyzing PMS. Considering the excellent properties of natural kaolinite (low cost, abundance, stability, etc.), it is a promising catalyst of PMS for effective degradation of highly toxic contaminants. This study provides useful insights and new strategies for PMS activation for water and wastewater treatment.

Acknowledgements

The authors gratefully acknowledge the financial support provided by Fundamental Research Funds for the Central Universities (2015QH01 and 2010YH10), the Young Elite Scientists Sponsorship Program by CAST (2017QNRC001) and Yueqi Funding Scheme for Young Scholars (China university of Mining & Technology, Beijing). The first author thanks the China Scholarship Council (CSC) for financial support (201706430019). Ying Huang also acknowledges support from the China Scholarship Council (CSC) scholarship (201306270057). D. D. Dionysiou acknowledges support from the University of Cincinnati



Scheme 1. The diagram of the possible activation mechanism and the potential radicals' transfer and transform routes.

through a UNESCO co-Chair Professor position on “Water Access and Sustainability” and the Herman Schneider Professorship in the College of Engineering and Applied Sciences.

Appendix A. Supplementary data

Supplementary material related to this article can be found, in the online version, at doi:<https://doi.org/10.1016/j.apcatb.2019.01.079>.

References

- [1] W. Hua, E.R. Bennett, R.J. Letcher, *Water Res.* 40 (2006) 2259–2266.
- [2] W.W. Tang, G.M. Zeng, J.L. Gong, Y. Liu, X.Y. Wang, Y. Liu, Z.F. Liu, L. Chen, X.R. Zhang, D.Z. Tu, *Chem. Eng. J.* 211–212 (2012) 470–478.
- [3] K.V. Plakas, A.J. Karabelas, J. *Membr. Sci.* 320 (2008) 325–334.
- [4] G.R. Malpass, D.W. Miwa, A.C. Miwa, S.A. Machado, A.J. Motheo, *Environ. Sci. Technol.* 41 (2007) 7120–7125.
- [5] A. Joss, S. Zabczynski, A. Göbel, B. Hoffmann, D. Löffler, C.S. Mcardell, T.A. Ternes, A. Thomsen, H. Siegrist, *Water Res.* 40 (2006) 1686–1696.
- [6] T. An, H. Yang, G. Li, W. Song, W.J. Cooper, X. Nie, *Appl. Catal. B: Environ.* 94 (2010) 288–294.
- [7] F.J. Rivas, M. Carbajo, F. Beltrán, O. Gimeno, J. Frades, *J. Hazard. Mater.* 155 (2008) 407–414.
- [8] C. Li, Z. Sun, W. Zhang, C. Yu, S. Zheng, *Appl. Catal. B: Environ.* 220 (2018) 272–282.
- [9] R. Yuan, S.N. Ramjaun, Z. Wang, J. Liu, *J. Hazard. Mater.* 196 (2011) 173–179.
- [10] F. Ghanbari, M. Moradi, *Chem. Eng. J.* 310 (2017) 41–62.
- [11] W. Li, P.X. Wu, Y. Zhu, Z.J. Huang, Y.H. Lu, Y.W. Li, Z. Dang, N.W. Zhu, *Chem. Eng. J.* 279 (2015) 93–102.
- [12] Y. Wang, Z. Ao, H. Sun, X. Duan, S. Wang, *Appl. Catal. B: Environ.* 198 (2016) 295–302.
- [13] H. Sun, Y. Wang, S. Liu, L. Ge, L. Wang, Z. Zhu, S. Wang, *Chem. Commun.* 49 (2013) 9914–9916.
- [14] S. Zhu, X. Huang, F. Ma, L. Wang, X. Duan, S. Wang, *Environ. Sci. Technol.* 52 (2018) 8649–8658.
- [15] X. Duan, H. Sun, S. Wang, *Acc. Chem. Res.* 51 (2018) 678–687.
- [16] C. Cai, H. Zhang, X. Zhong, L. Hou, *J. Hazard. Mater.* 283 (2015) 70–79.
- [17] H. Song, L. Yan, J. Jiang, J. Ma, Z. Zhang, J. Zhang, P. Liu, Y. Yang, *Water Res.* 128 (2017) 393–401.
- [18] L. Li, D. Zhang, C. Fan, C. Shang, *Water Res.* 124 (2017) 446–453.
- [19] C. Li, Z. Sun, R. Ma, Y. Xue, S. Zheng, *Microporous Mesoporous Mater.* 243 (2017) 281–290.
- [20] Y.H. Chen, D.L. Lu, *Appl. Clay Sci.* 104 (2015) 221–228.
- [21] J. Wang, S. Xia, L. Yu, *Appl. Surf. Sci.* 339 (2015) 28–35.
- [22] X. Duan, T. Sanan, A. de la Cruz, X. He, M. Kong, D.D. Dionysiou, *Environ. Sci. Technol.* 52 (2018) 8252–8262.
- [23] N. Wahba, M. El Asmar, M. El Sad, *Anal. Chem.* 31 (1959) 1870–1871.
- [24] S. Cheng, X. Zhang, Y. Yang, C. Shang, W. Song, J. Fang, Y. Pan, *Environ. Sci. Technol.* 52 (2018) 1806–1816.
- [25] X. He, S.P. Mezyk, I. Michael, D. Fatta-Kassinos, D.D. Dionysiou, *J. Hazard. Mater.* 279 (2014) 375–383.
- [26] Y. Huang, C. Han, Y. Liu, M.N. Nadagouda, L. Machala, K.E. O’Shea, V.K. Sharma, D.D. Dionysiou, *Appl. Catal. B: Environ.* 221 (2018) 380–392.
- [27] C. Belver, M.A. Vicente, *Chem. Mater.* 14 (2002) 2033–2043.
- [28] Z. Sun, C. Li, X. Du, S. Zheng, G. Wang, *J. Colloid Interface Sci.* 511 (2018) 268–276.
- [29] E.F. Aglietti, J.M. Porto Lopez, E. Pereira, *Appl. Clay Sci.* 3 (1988) 155–163.
- [30] A. Steudel, L.F. Batenburg, H.R. Fischer, P.G. Weidler, K. Emmerich, *Appl. Clay Sci.* 44 (2009) 95–104.
- [31] X. Li, Q. Liu, H. Cheng, S. Zhang, R.L. Frost, *J. Colloid Interface Sci.* 444 (2015) 74–80.
- [32] C. Li, Z. Sun, X. Li, L. Liu, S. Zheng, *Adv. Powder Technol.* 27 (2016) 2051–2060.
- [33] T.L. Barr, S. Seal, H. He, J. Klinowski, *Vacuum* 46 (1995) 1391–1395.
- [34] C. Li, Z. Sun, A. Song, X. Dong, S. Zheng, D.D. Dionysiou, *Appl. Catal. B: Environ.* 236 (2018) 76–87.
- [35] H. Lin, J. Wu, H. Zhang, *Chem. Eng. J.* 244 (2014) 514–521.
- [36] R. Yin, W. Guo, H. Wang, J. Du, X. Zhou, Q. Wu, H. Zheng, J. Chang, N. Ren, *Chem. Eng. J.* 335 (2018) 145–153.
- [37] Y. Wang, H. Sun, H.M. Ang, M.O. Tadé, S. Wang, *Appl. Catal. B: Environ.* 164 (2015) 159–167.
- [38] Y.F. Huang, Y.H. Huang, *J. Hazard. Mater.* 167 (2009) 418–426.
- [39] C. Li, Z. Sun, L. Liu, W. Huang, S. Zheng, *RSC Adv.* 6 (2016) 91002–91011.
- [40] Y.H. Guan, J. Ma, X.C. Li, J.Y. Fang, L.W. Chen, *Environ. Sci. Technol.* 45 (2011) 9308–9314.
- [41] J. Deng, Y.Q. Cheng, Y.A. Lu, J.C. Crittenden, S.Q. Zhou, N.Y. Gao, J. Li, *Chem. Eng. J.* 330 (2017) 505–517.
- [42] X. Duan, C. Su, J. Miao, Y. Zhong, Z. Shao, S. Wang, H. Sun, *Appl. Catal. B: Environ.* 220 (2018) 626–634.
- [43] Y. Guo, X. Lou, C. Fang, D. Xiao, Z. Wang, J. Liu, *Environ. Sci. Technol.* 47 (2013) 11174–11181.
- [44] Y. Xu, J. Ai, H. Zhang, *J. Hazard. Mater.* 309 (2016) 87–96.
- [45] Y. Xu, H. Lin, Y. Li, H. Zhang, *Sci. Total Environ.* 609 (2017) 644–654.
- [46] Y. Xu, A. Jia, H. Zhang, *J. Hazard. Mater.* 309 (2016) 87–96.
- [47] R. Luo, C. Liu, J. Li, J. Wang, X. Hu, X. Sun, J. Shen, W. Han, L. Wang, *J. Hazard.*

- Mater. 329 (2017) 92–101.
- [48] Y. Yang, J. Jiang, X. Lu, J. Ma, Y. Liu, Environ. Sci. Technol. 49 (2015) 7330–7339.
- [49] Y.H. Guan, J. Ma, Y.M. Ren, Y.L. Liu, J.Y. Xiao, L.Q. Lin, C. Zhang, Water Res. 47 (2013) 5431–5438.
- [50] J. Zhang, X. Shao, C. Shi, S. Yang, Chem. Eng. J. 232 (2013) 259–265.
- [51] Y. Ding, L. Zhu, N. Wang, H. Tang, Appl. Catal. B: Environ. 129 (2013) 153–162.
- [52] C. Chen, S. Yang, Y. Guo, C. Sun, C. Gu, B. Xu, J. Hazard. Mater. 172 (2009) 675–684.
- [53] Z. Zhou, M.H. Liu, Q.S. Cao, X.D. Zhu, Mod. Chem. Ind. 37 (2017) 83–87.
- [54] W.-D. Oh, S.-K. Lua, Z. Dong, T.-T. Lim, J. Mater. Chem. A 2 (2014) 15836–15845.
- [55] H. Al-Hosney, V. Grassian, Phys. Chem. Chem. Phys. 7 (2005) 1266–1276.
- [56] T. Zhang, H. Zhu, J.-P. Croué, Environ. Sci. Technol. 47 (2013) 2784–2791.
- [57] Y. Wang, Z. Ao, H. Sun, X. Duan, S. Wang, Appl. Catal. B: Environ. 198 (2016) 295–302.
- [58] X. Duan, Z. Ao, H. Zhang, M. Saunders, H. Sun, Z. Shao, S. Wang, Appl. Catal. B: Environ. 222 (2018) 176–181.